nature catalysis

Article

https://doi.org/10.1038/s41929-023-00990-9

Activation of light alkanes at room temperature and ambient pressure

Received: 10 October 2022

Accepted: 21 June 2023

Published online: 20 July 2023

Check for updates

Haochen Zhang[1,5], Chunsong Li[1,5], Wenxuan Liu[1], Guangsheng Luo[1], William A. Goddard III[2], Mu-Jeng Cheng[3], Bingjun Xu[4] ✉ & Qi Lu[1] ✉

Light alkane activation under mild conditions remains a substantial challenge. Here we report an aqueous reaction system capable of selectively converting light alkanes into corresponding olefins and oxygenates at room temperature and ambient pressure using Cu powder as the catalyst and O_2 as the oxidant. In ethane activation, we achieved a combined production of ethylene and acetic acid at a rate of 2.27 mmol g_{Cu}^{-1} h^{-1}, with a combined selectivity up to 97%. Propane is converted to propylene with a selectivity up to 94% and a production rate up to 1.83 mmol g_{Cu}^{-1} h^{-1}, while methane is converted mainly to carbon dioxide, methanol and acetic acid. On the basis of catalytic experiments, isotopic labelling experiments, spectroscopic insights and density functional theory calculations, we put forward mechanistic understandings in which the C–H bond is activated by the surface oxide species generated during the oxidation process, forming alkyl groups as key reaction intermediates.

The production of light alkanes, that is, methane, ethane and propane, has been boosted due to the development of shale gas exploitation. The direct conversion of these hydrocarbons into high-value liquid fuels and commodity chemicals under mild conditions is an economically promising but fundamentally challenging route for on-site utilization and storage of these resources[1,2]. Elevated temperatures (200–600 °C) and pressures (typically 5–50 bar) are typically required to promote these reactions, such as the dehydrogenation and cracking of ethane and propane to produce olefins[3–5] as well as the partial oxidation of light alkanes to oxygenates via gas-phase chemical looping[6–8]. Large-scale, centralized plants are needed to make these processes profitable, which hinders the exploitation of light alkanes produced at remote oil or gas fields. Electrophilic metal cations were found to activate light alkanes at less critical conditions (110–220 °C, 10–35 bar) to form corresponding alcohol esters[9–12]. However, corrosive solvents (oleum or trifluoroacetic acid) are required to facilitate the reaction and protect the products against overoxidation. Additional hydrolysis steps are also needed to convert produced esters into desired alcohols, which increases the operational cost of the process.

On-site utilization of light alkanes necessitates the development of processes that are convenient and operate under mild conditions. In this Article, we demonstrate an aqueous system for the light alkane activation that is capable of converting these hydrocarbons into corresponding oxygenates and olefins under room temperature and ambient pressure with Cu as the catalyst and gaseous O_2 as the oxidant. In particular, ethane can be partially oxidized to ethylene and acetic acid with a conversion rate of 2.27 mmol g_{Cu}^{-1} h^{-1} and a combined selectivity up to 97%. Propane can be converted to propylene with a rate up to 1.83 mmol g_{Cu}^{-1} h^{-1} and a selectivity up to 94%. The main products of methane activation are carbon dioxide, methanol and acetic acid. Isotopic labelling experiments and in situ surface-enhanced Raman spectroscopy (SERS) were conducted to probe key reaction intermediates, and the reaction mechanism was investigated using density functional theory (DFT) calculations.

Results

Activation of light alkanes by copper powder

The activation of light alkanes was conducted by co-feeding one alkane (that is, ethane, propane or methane) and O_2 into a magnetically stirred

[1]State Key Laboratory of Chemical Engineering, Department of Chemical Engineering, Tsinghua University, Beijing, China. [2]Materials and Process Simulation Center, California Institute of Technology, Pasadena, CA, USA. [3]Department of Chemistry, National Cheng Kung University, Tainan, Taiwan. [4]College of Chemistry and Molecular Engineering, Peking University, Beijing, China. [5]These authors contributed equally: Haochen Zhang, Chunsong Li. ✉e-mail: b_xu@pku.edu.cn; luqicheme@mail.tsinghua.edu.cn

https://doi.org/10.1038/s41929-023-00990-9

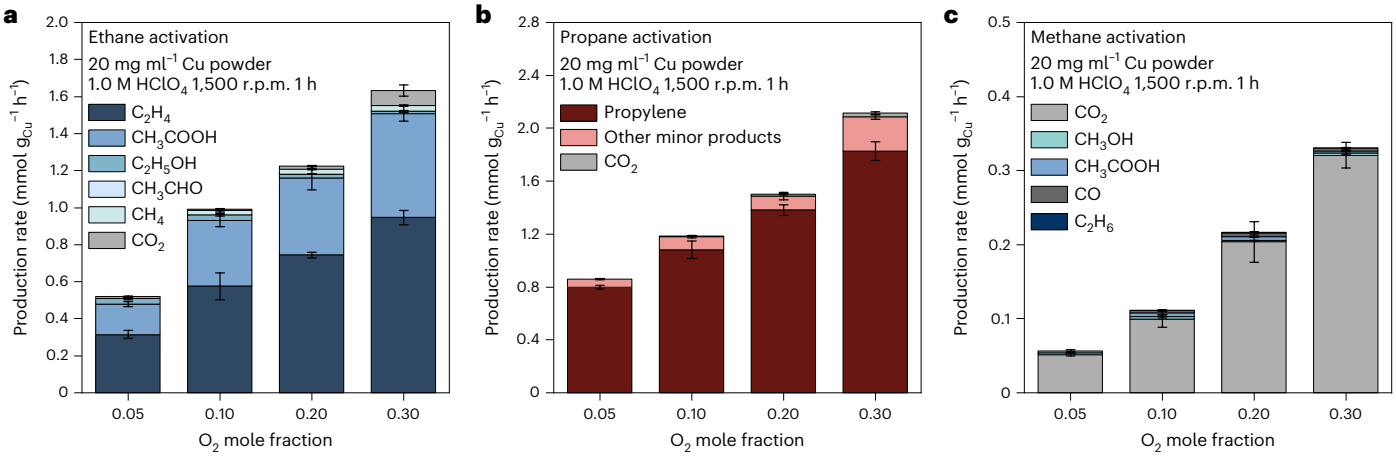

Fig. 1 | Light alkane activation with different O_2 mole fractions in the feed at room temperature. a–c, The production rate and distribution of ethane activation (**a**), propane activation (**b**) and methane activation (**c**) with different mole fractions of O_2 in the gas feed. The stirring rate was 1,500 r.p.m. Total pressure in the reactor was 1 atm consisting of alkane and O_2. Error bars represent the standard deviation of four independent measurements, and the data are presented as mean ± standard deviation.

Cu powder suspension prepared by dispersing Cu powder into an aqueous $HClO_4$ solution at room temperature and ambient pressure (for experimental details, see Methods). Scanning electron microscopy (SEM) analysis showed that Cu powders were several micrometres in size (Supplementary Fig. 1). Powder X-ray diffraction patterns exhibited peaks at the expected positions for the bulk Cu lattice with an estimated average crystalline size of 39 nm using the Scherrer equation (Supplementary Fig. 2). The specific surface area is 2.3 $m^2 g^{-1}$ measured by the Brunauer–Emmett–Teller isotherm. X-ray photoelectron spectroscopy (XPS) data indicated the existence of native oxides on the surface, which was probably due to the inevitable exposure to atmospheric air (Supplementary Fig. 3). In $HClO_4$ solution, these native surface Cu oxides were quickly removed under Ar as shown in the in situ SERS investigations (Supplementary Fig. 4).

Figure 1a shows the results of ethane activation at room temperature and ambient pressure at different mole ratios of C_2H_6 and O_2 in 1.0 M $HClO_4$ with a Cu powder loading of 20 mg per millilitre of solution. The main products are ethylene in the gas phase and acetic acid in the liquid phase, with small amounts of ethanol, acetaldehyde, methane and carbon dioxide (Supplementary Fig. 5 and Supplementary Table 1). The rates of major products increase as the mole fraction of O_2 in the gas feed increases from 0.05 to 0.30, while the ethane mole fraction decreases concomitantly, indicating a positive reaction order of O_2 in activating ethane. At an O_2 mole fraction of 0.30, we achieved optimal production rates of 0.95 mmol $g_{Cu}^{-1} h^{-1}$ for ethylene and 0.56 mmol $g_{Cu}^{-1} h^{-1}$ for acetic acid, respectively. The concentration of acetic acid reached 11.2 mM under this condition after 1 h of reaction, highlighting that this process could produce quantities of oxygenates with practical importance. The rates of ethane activation continue to raise with further increase in the O_2 mole fraction in the gas feed up to 0.5 (Supplementary Fig. 6). No product was observed if either ethane or Cu powder was absent in the reaction system (Supplementary Fig. 7 and Supplementary Table 2). Trace amounts of ethylene, acetic acid and ethanol were detected in control experiments without O_2 feed (that is, <1% of the production with O_2 mole fraction of 0.2), which we attribute to a slight filtration of ambient air into the system during reactions (Supplementary Fig. 7 and Supplementary Table 2). These results confirm that the products originate from ethane conversion in the presence of O_2 and Cu powder.

Figure 1b shows the results of propane activation at otherwise identical conditions (for minor product distributions, see Supplementary Fig. 8). The main product of propane activation is propylene with a selectivity up to 94% (Supplementary Table 3). The conversion rate of propane also increases with increased O_2 mole fraction in the feed. At the O_2 mole fraction of 0.30, the production rate of propylene reached 1.83 mmol $g_{Cu}^{-1} h^{-1}$ with the selectivity of 88%. Other minor products, including propionic acid, acetone, allyl alcohol, 3-hydroxypropionic acid and acetic acid, were also detected. The mass-specific reaction rate of our ethane and propane activation at ambient conditions is comparable to the results in literature that are obtained at elevated temperature (comparisons provided in Supplementary Tables 4 and 5).

For co-feeding methane and O_2, CO_2 is the main product, with a production rate that also increases with increased O_2 mole fractions (Fig. 1c and Supplementary Table 6). Methanol, acetic acid and CO were also identified with production rates of 3.0, 2.7 and 4.0 μmol $g_{Cu}^{-1} h^{-1}$, respectively, at an O_2 mole fraction of 0.3. A trace amount of ethane was also detected. These results indicate that ample methyl species (identified below) are available on the Cu surface for coupling reactions. The ethane produced from methane activation could also be further converted to ethylene in our system. However, the concentration of ethane from methane activation is very low (with partial pressure of ethane less than 0.001 atm), and thus its conversion to ethylene is too low to be detected.

We note that transition metal ions are capable of catalytically decomposing H_2O_2 to generate powerful oxidizing radicals (that is, Fenton reaction). In our system, the reaction of O_2 and metallic Cu in solution might produce H_2O_2 and the possible subsequent decomposition of the produced H_2O_2 by Cu ions could generate such radicals that might play a role in the oxidation sequence. If H_2O_2 were formed by the aerobic oxidation of Cu(0), the upper bound of H_2O_2 concentration could be calculated to be 0.18 M on the basis of the Cu^{2+} concentration after a typical 1 h ethane activation reaction. Thus, we performed control experiments with 0.2 M H_2O_2 as the oxidant instead of O_2 in ethane activation. As shown in Supplementary Fig. 9, the reaction rate using 0.2 M H_2O_2 is less than 10% of that using O_2 as the oxidant under otherwise identical conditions, with detailed data provided in Supplementary Table 2. Therefore, we believe that Cu-catalysed Fenton pathway is unlikely to be the reaction mechanism in our system. As noble metals (that is, Pt and Pd) are capable of catalysing aerobic oxidation of alcohols, we also conducted control experiments with 20 mg ml^{-1} Pt or Pd powder with similar dimensions to Cu powder under otherwise identical conditions. As shown in Supplementary Fig. 10, only trace amounts of products were detected (detailed data are provided in Supplementary Table 2).

https://doi.org/10.1038/s41929-023-00990-9

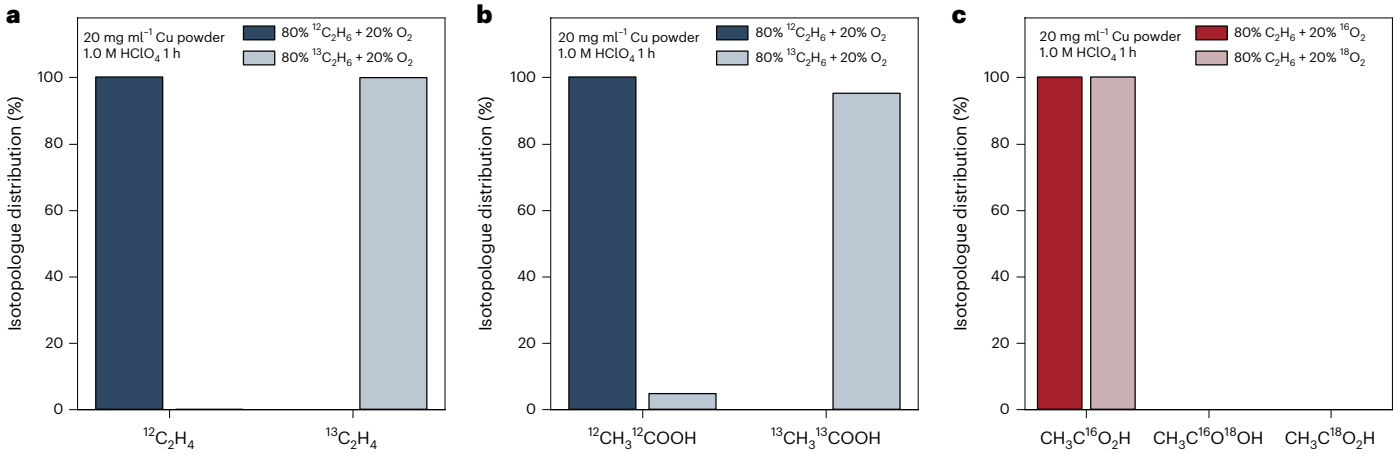

Fig. 2 | Isotopic labelling investigation of ethane activation. a–c, Isotopologue distributions of produced ethylene (**a**) and acetic acid (**b**) using $^{13}C_2H_6$ or $^{12}C_2H_6$ in the gas feed, and acetic acid using $^{18}O_2$ or $^{16}O_2$ in the gas feed (**c**). A tiny amount of ^{12}C acetic acid (1.6% of total products detected) was observed with $^{13}C_2H_6$ gas feed, which is probably due to ^{12}C contaminations in the $^{13}C_2H_6$ cylinder. The stirring rate was 1,500 r.p.m. Total pressure in the reactor was 1 atm consisting of C_2H_6 and O_2.

Isotope-labelled ethane ($^{13}C_2H_6$) and O_2 ($^{18}O_2$) were used as the gas feed to probe the carbon and oxygen source of major products from ethane activation. The ^{13}C-labelled ethylene was quantified using gas chromatography–mass spectrometry (GC–MS), and ^{13}C-labelled and ^{18}O-labelled acetic acid were quantified using both proton nuclear magnetic resonance (NMR) and GC–MS. The GC–MS profiles and NMR spectra are provided in Supplementary Figs. 11–13. As shown in Fig. 2a,b, all major products are ^{13}C-labelled when $^{13}C_2H_6$ was used as the gas feed, confirming that the carbon source of observed products is ethane. Interestingly, no acetic acid is ^{18}O-labelled when $^{18}O_2$ was used (Fig. 2c), indicating that water, rather than gaseous O_2, is the oxygen source for the oxygenates produced from ethane activation. This is consistent with the mechanism we proposed based on DFT calculations, which will be discussed in the following sections. The ^{18}O-labelling results also exclude the possibility that oxygenates are produced from the reaction between ethyl and hydroxyl radicals which originate from O_2 via Fenton-like mechanism, in which oxygen atoms from O_2 would incorporate into produced oxygenates.

We then investigated the impact of $HClO_4$ concentration and Cu powder loading on the reaction performance in ethane activation due to its relatively high reaction rate and simple product distribution. The production rate increases substantially (by a factor of 3) with increasing $HClO_4$ concentration from 0.1 to 0.5 M, and then plateaus for further concentrations to 2.0 M (Fig. 3a and Supplementary Table 7). This behaviour suggests that the reaction is probably limited by mass transport of ethane or O_2 at $HClO_4$ concentrations higher than 0.5 M. Replacing 1.0 M $HClO_4$ with 1.0 M $NaClO_4$ leads to only trace amounts of products, highlighting the role of proton in the activation (Supplementary Fig. 14 and Supplementary Table 2). Perchlorate is unlikely to act as an oxidant, since replacing $HClO_4$ with H_2SO_4 results in comparable reaction rates and product distributions (Supplementary Fig. 14 and Supplementary Table 2). Weaker acid solutions, including 1.0 M H_3PO_4 and 1.0 M $H_2C_2O_4$, were also tested for ethane activation (Supplementary Fig. 14 and Supplementary Table 2). For H_3PO_4, ethylene and acetic acid were produced but less than those produced in $HClO_4$. This could be due to the formation of insoluble $Cu_3(PO_4)_2$ on Cu surface in H_3PO_4, which could block the Cu surface. As for oxalic acid, no product but substantial amount of CO_2 was observed. This is probably due to the oxidation of oxalic acid is favoured over ethane in our system.

The loading of Cu powder also influences the reaction performance (Fig. 3b and Supplementary Table 8). As the loading of Cu powder is doubled from 5 to 10 mg ml^{-1}, the apparent ethane conversion rate doubles, while further increasing this loading to 40 mg ml^{-1} results in only negligible changes, indicating that the reaction becomes limited by mass transport of the reactants. The total production rates normalized by the Cu mass are nearly identical at Cu powder loadings of 5 mg ml^{-1} and 10 mg ml^{-1} with the highest combined production rate of ethylene and acetic acid of 2.27 mmol g_{Cu}^{-1} h^{-1} achieved at 10 mg ml^{-1}, but decreases at higher loadings, suggesting that mass transport of reactants to the Cu surface increasingly becomes a limiting factor in our current reaction configuration with O_2 mole fraction of 0.2. As expected, higher stirring rates increase the rate of ethane activation (Supplementary Fig. 15 and Supplementary Table 9).

Cu dissolves in the O_2-containing acid solution. At O_2 mole fraction of 0.2, the loading of Cu powder decreases from 20 mg ml^{-1} to approximately 8 mg ml^{-1} in 1 h ethane activation reaction. The dissolution rate of Cu is 1.8 mmol h^{-1} under this condition, approximately 7.5 times higher than ethane activation rate (Supplementary Table 10). While the higher O_2 mole fraction promotes the ethane activation rate (Fig. 1a and Supplementary Fig. 6), it also expedites the Cu dissolution (Supplementary Fig. 16a), resulting in the time-dependent reaction rate reducing more rapidly within 1 h reaction (Supplementary Fig. 16b). The dissolved Cu can be recycled from the post-reaction solution using electrolysis and reused as the catalyst in practical applications. As a proof-of-concept demonstration, we performed three consecutive ethane activation experiments in which the latter two used the recycled Cu electrolysed from the solution of the preceding experiment as the catalyst (for experimental details, see Methods). As the results show in Supplementary Fig. 17, the recycled Cu exhibited similar reactivity in ethane activation as the fresh Cu, and the Cu recycling efficiency is higher than 95% for each recycle process. We note that Cu^{2+} salts were reported to catalyse alkane oxidation in the presence of O_2 and aldehydes to produce corresponding alcohols and ketones in dichloromethane under mild conditions[13,14]. In this system, 0.5 M aldehydes react with O_2 in the presence of 5 mM Cu^{2+} salts, producing peracids that subsequently react with Cu^{2+} salts to afford active oxygen-containing copper species capable of breaking the C–H bonds in the alkanes. Although trace amount of acetaldehyde is detected as a minor product in our system, the concentration of produced acetaldehyde is too low to contribute to ethane activation even if acetaldehyde could serve as the catalyst in a similar manner. To examine the possible role of Cu^{2+} from Cu dissolution in our system, we performed control experiments with Cu^{2+} solution as the reaction medium without Cu powder, confirming that aqueous Cu^{2+} was not responsible for ethane activation (Supplementary Fig. 7 and Supplementary Table 2). The ^{18}O-labelling results also suggest that O_2 is not the oxygen source for produced oxygenates,

https://doi.org/10.1038/s41929-023-00990-9

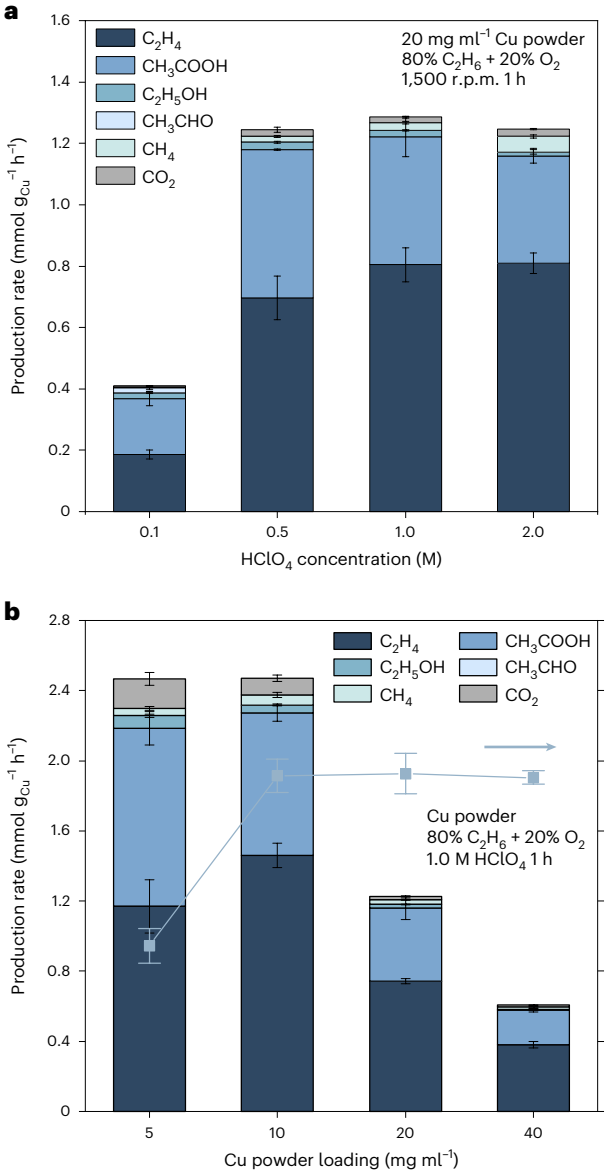

Fig. 3 | Rate and product distribution of ethane activation. a,**b**, Production rate and distribution of ethane activation with different $HClO_4$ concentrations (**a**) and with different Cu powder loadings (**b**). Error bars represent the standard deviation of four independent measurements, and the data are presented as mean ± standard deviation.

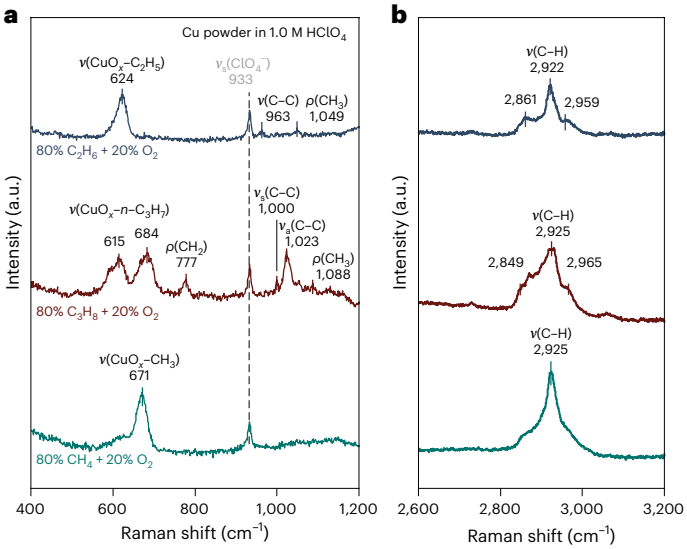

Fig. 4 | In situ SERS of ethane, propane and methane activation. a, Raman spectra in the range from 400 to 1,200 cm^{-1}. **b**, Raman spectra in the range from 2,600 to 3,200 cm^{-1}. The mole ratio of alkane and O_2 is 8:2.

which differs from the aldehyde-catalysed mechanism where oxygen atoms from O_2 are incorporated into the final products (Fig. 2c)[13,14].

In situ SERS

We identified adsorbed alkyl groups with in situ SERS during alkane activation conditions (for experimental details, see Methods). Cu powder readily exhibit surface enhancement of Raman signals, alleviating the need to roughen the surface or the introduction of SERS-inducing particles[15]. A peak at 933 cm^{-1} was observed in all experiments which we attribute to the symmetrical stretching mode of perchlorate ion ($\nu_s(ClO_4^-)$) (Fig. 4a)[16]. For ethane activation, we observed a strong peak at 624 cm^{-1} accompanied by weak peaks at 963 and 1,049 cm^{-1} (Fig. 4a) and intense peaks at 2,861, 2,922 and 2,959 cm^{-1} (Fig. 4b). The absence of these bands in a pure ethane or pure O_2 feed indicates that they are not correlated to surface-adsorbed ethane, surface oxygen or bare Cu oxide species generated from the reaction between Cu and O_2 (Supplementary Fig. 18)[17,18], while the rapid appearance of the Raman bands upon introduction of alkane and O_2 indicates that the corresponding species are related to alkane activation. Replacing H_2O with D_2O does not impact the position of these peaks, suggesting that the corresponding species do not contain any exchangeable H(D) (Supplementary Fig. 19). We attribute the peaks at 963, 1,049 cm^{-1} to the C–C bond stretching mode (ν(C–C)) and the methyl group rocking mode ($\rho(CH_3)$), respectively[19–21], while we assign bands at 2,861, 2,922 and 2,959 cm^{-1} to the C–H bond stretching modes (ν(C–H))[20–22].

To probe the nature of the band centred at 624 cm^{-1}, we conducted control experiments using ethanol and iodoethane (Supplementary Fig. 20). No Raman features appear in the ethanol-containing (50 mM) $HClO_4$ (1.0 M) except for those of perchlorate, suggesting the observed bands are not associated with molecular or dissociative adsorption of ethanol (Supplementary Fig. 20a)[23]. Iodoethane is known to dissociate and form ethyl groups[21,24]. The Raman spectrum with 50 mM iodoethane exhibits bands at 625, 962 and 1,048 cm^{-1} similar to the spectrum under ethane activation conditions (Fig. 4a and Supplementary Fig. 20b). Replacing C_2H_5I with C_2D_5I leads to a redshift of 625 to 577 cm^{-1}, suggesting it is correlated with a H(D)-containing species (Supplementary Fig. 21a). No Cu–C stretch modes (typically associated with alkyl-bound Cu metals) were observed[22,25,26]. These spectral observations together suggest that the peak at 624 cm^{-1} can be assigned to the CuO_x–C_2H_5 species since the Cu surface is expected to be oxidized under such oxidative conditions. We note that Cu oxide is thermodynamically unstable in acidic solutions, and thus the oxide-associated Raman bands disappear when 1.0 M $HClO_4$ is introduced to the Cu catalysts under Ar atmosphere (Supplementary Fig. 4). It is likely that, when alkanes are present in the reaction system and form hydrophobic surface alkyl groups from the C–H bond cleavage, the approach of solvated protons to the catalyst surface is hindered. This would retard the dissolution of surface Cu oxide that can be observed in SERS. This is consistent with the observation that the Cu dissolution is partially suppressed at the presence of alkane in the O_2-containing 1.0 M $HClO_4$ (Supplementary Table 10).

Similarly, the corresponding Raman features for alkyl groups were identified in propane and methane with the aid of alkyl iodides, alcohols and deuterated compounds. With the exception of $\nu_s(ClO_4^-)$ at 933 cm^{-1}, the Raman peaks in propane and methane activation appear only when alkane and O_2 are delivered simultaneously, similar to the case of ethane activation (Fig. 4a,b and Supplementary Fig. 18). The spectrum of propane activation exhibits identical bands as that with

https://doi.org/10.1038/s41929-023-00990-9

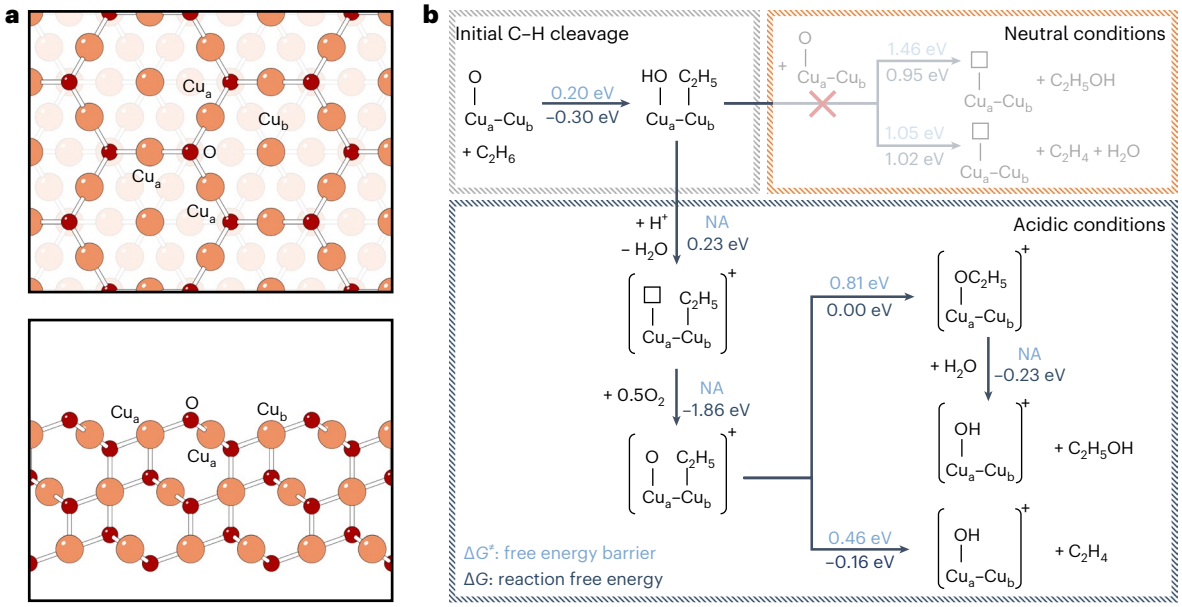

Fig. 5 | Theoretical investigations on the mechanism for ethane activation. a, Computational model of Cu_2O where orange and red spheres stand for Cu and O atoms, respectively. **b**, Possible reaction pathways towards ethylene and ethanol from ethane activation where the white square symbol stands for an oxygen vacancy and NA stands for no free energy barrier.

1-iodopropane rather than 2-iodopropane, suggesting that the primary C–H bonds of propane are activated first (Fig. 4a and Supplementary Fig. 20b). We assign: the peaks at 615, 684 cm^{-1} to the CuO_x–*n*–C_3H_7 species, the peaks at 777 and 1,088 cm^{-1} to the rocking mode of CH_2 ($\rho(CH_2)$) and CH_3 ($\rho(CH_2)$) groups[27], and the peaks at 1,000 and 1,023 cm^{-1} to the symmetric (ν_s(C–C)) and asymmetric (ν_a(C–C)) stretching mode of C–C bonds, respectively[25].

The spectrum of methane activation is nearly identical with that of the control experiment using iodomethane (Fig. 4a and Supplementary Fig. 20b). The peak at 671 cm^{-1} exhibits a redshift to 640 cm^{-1} when replacing CH_3I with CD_3I (Supplementary Fig. 21b), which we assign to the CuO_x–CH_3 species. In control experiments using alcohols of 1-propanol, 2-propanol and methanol, only $\nu_s(ClO_4^-)$ at 933 cm^{-1} can be observed, dismissing the possibility that the observed bands are due to adsorbed alcohols or alkoxides (Supplementary Fig. 20a).

To gain insights into the reaction pathway after the initial C–H bond cleavage, we used ethylene, ethanol and acetic acid as the substrate, rather than ethane, in 1.0 M $HClO_4$ with Cu powder loading of 20 mg ml^{-1} and O_2 mole fraction of 0.2 (for experimental details, see Methods). No ethylene conversion was observed suggesting that ethylene was not an intermediate en route to oxygenates or CO_2 in ethane activation (Supplementary Fig. 22 and Supplementary Table 2). With 10 mM ethanol, we detected acetaldehyde and acetic acid with reaction rates of 0.005 and 0.97 mmol g_{Cu}^{-1} h^{-1}, respectively (Supplementary Table 2). The similar distribution of these products to those of ethane activation indicates that ethanol is a key reaction intermediate towards these products in a sequential oxidation pathway. Interestingly, ethylene was also observed as a minor product in ethanol oxidation. However, the mole ratio of ethylene and acetic acid produced from ethanol oxidation (that is, 0.16) was substantially smaller than that from ethane activation (that is, 1.8), suggesting that ethanol is not likely to be an intermediate for the major ethylene production in ethane activation. We then conducted additional control experiments of ethanol oxidation with $^{18}O_2$. No ^{18}O-labelled acetaldehyde or acetic acid was observed, which is consistent with the results of ethane activation (Supplementary Fig. 23). The primary product in acetic acid oxidation is CO_2, which is also observed in ethanol oxidation but with a much lower rate than in acetic acid oxidation under otherwise identical conditions (Supplementary Table 2). Therefore, CO_2 from ethane activation probably originates from oxidation of the produced acetic acid. We note that the selectivity towards CO_2 in ethane activation is relatively low (<4%) in all reaction conditions evaluated. The total reaction rate of ethane activation is also higher than that of ethanol and acetic acid oxidation. This could be because the C–H bond cleavage occurs via an electrophilic oxidation by the surface Cu(I) induced by O_2 in our system. Similar mechanisms were reported in previous literatures on Pd, Hg and Rh ions[9,28–30]. In electrophilic oxidation, the C–H bond with higher electron density is easier to be cleaved. The C–H bond within ethane has a higher electron density compared with other substrates including ethanol and acetic acid due to their oxygen-containing electron-withdrawing groups, and thus the oxidation of ethane can be more facile than ethanol or acetic acid. Decarboxylation is another possible pathway for acetic acid oxidation to CO_2. However, the products formed for both ethane and propane activation suggest that decarboxylation is not favoured in this system, so the underlying mechanism requires further investigations.

Computational investigations on reaction mechanism

DFT and molecular dynamics (MD) simulations were carried out to further investigate the possible mechanisms of alkane activation in this system (atomic coordinates of optimized computational models can be found in Supplementary Data 1 and 2). Our ReaxFF MD simulations suggested that a thin Cu oxide layer would form on Cu surface in contact with gaseous O_2 (Supplementary Fig. 24), which is consistent with previous scanning tunnelling microscopy and electron energy loss spectroscopy studies that also reveal the existence of a Cu_2O oxide layer[31,32]. Cu_2O with two or more atomic layers is known to exhibit bulk properties[33]. Thus, we chose Cu_2O as the model surface for DFT calculations (Fig. 5a). Figure 5b shows the energy diagram for ethane activation to produce ethylene and ethanol. The first step for all possible pathways is initial C–H bond cleavage to produce a Cu-bound ethyl group and a hydroxyl group (scheme of structures shown in Supplementary Fig. 25). This step is spontaneous with a free energy barrier of only 0.20 eV, easily surmounted under ambient conditions. Moreover, free energy barriers for the initial C–H bond cleavage for methane and propane are only 0.20 eV and 0.23 eV, respectively. This is consistent with our spectroscopic results that the first C–H bond

activation in alkane is facile and forms stable adsorbed alkyl groups on the surface. In contrast, the reaction free energy barrier for ethane activation on metallic Cu is calculated to be as high as 1.32 eV, suggesting that metallic Cu is unlikely to be the reaction centre. Under neutral conditions, further C–H bond cleavage or C–O bond formation of the formed ethyl group leading to production of ethylene or ethanol is kinetically prohibited due to their considerably large free energy barriers of at least 1.05 eV (Fig. 5b and Supplementary Fig. 26). However, the presence of protons under acidic conditions can react with the surface hydroxyl group to form water and a positively charged surface with an oxygen vacancy, which can be quickly replenished with molecular oxygen (Fig. 5b). The further C–H bond cleavage or C–O bond formation on this positively charged surface is kinetically favoured with barriers of 0.46 eV and 0.81 eV, respectively (Fig. 5b and Supplementary Fig. 27). This is attributed to these two reactions involving a net electron transfer from the ethyl group to the surface (1.27 e and 0.93 e for every ethyl group reacted to form ethylene or ethanol, respectively, according to Bader charge analysis). Thus, the driving forces for these steps are larger on a positively charged surface than their counterparts at neutral conditions. The resulting protonated surface can then react with the acidic solvent to hydrate and then dissolve the Cu ions, exposing fresh Cu to react with O_2 to form Cu_2O surface for ethane activation. The reaction mechanism revealed by DFT calculations is in good agreement with our experimental results that ethylene and ethanol are not produced sequentially. In particular, ethanol is produced by the nucleophilic attack of ethoxy group by water, during which the oxygen atom of water forms a C–O bond with the ethyl group. This is consistent with the observation in isotopic labelling experiments that water, rather than gaseous O_2 is the oxygen source for the oxygenates produced from ethane activation. The DFT calculations also suggest that the protons can promote ethane activation effectively by coupling with the facile Cu dissolution reaction. This is consistent with our observation that the Cu dissolution is partially suppressed in the presence of ethane in the O_2-containing 1.0 M $HClO_4$ (Supplementary Table 10). The reduction in Cu dissolution rate when changing the feed from Ar/O_2 to $ethane/O_2$ (with the same mole ratio of 8:2) is comparable to the rate of ethane activation.

We also conducted control experiments using CuO (25 mg ml^{-1}) or Cu_2O (22.5 mg ml^{-1}) as the catalyst for ethane activation with or without O_2 feed. The mass loadings were chosen to keep the same concentration of Cu element (20 mg ml^{-1}) as in ethane activation using metallic Cu powder. As the results show in Supplementary Fig. 28, for CuO, only trace amounts of products could be detected regardless the presence of O_2 or not, indicating that CuO is inactive for ethane activation. For Cu_2O, while very limited products were detected in the absence of O_2, a production rate of ~32% of that in experiment using metallic Cu was observed at the presence of O_2 with major product of acetic acid. Detailed data are provided in Supplementary Table 2. These results demonstrate the critical role of O_2 in replenishing the oxygen vacancy for activating ethane on Cu_2O, as suggested by our DFT calculated reaction mechanism.

Conclusions

Our experimental and computational results demonstrate a reaction system capable of converting light alkanes to the corresponding oxygenates and olefins under room temperature and ambient pressure using commercial polycrystalline Cu powder as the catalyst and gaseous O_2 as the oxidant. By employing isotopic labelling experiments, in situ SERS and DFT calculations, we proposed a possible reaction mechanism with adsorbed alkyl groups as the reaction intermediates. Our system paves the way for selective C–H bond activation, offering opportunities for functionalizing light alkanes as well as other relatively inert but important organic compounds such as cyclohexane and octane, under mild conditions.

Methods

Light alkane activation

All light alkane activations were carried out in a homemade glass cell (Supplementary Fig. 29). De-ionized water in all experiments was from a Millipore system (18.2 MΩ cm). Copper powder (Sigma-Aldrich, dendritic, <45 μm, 99.7% trace metals basis) were firstly rinsed in 0.1 M $HClO_4$ (Aladdin, 70% $HClO_4$, 99.999% metals basis) for at least 15 min to remove native oxides before reactions. Then the suspension was allowed to settle for 5 min and the clear supernatant solution was discarded. Fresh 1.0 M $HClO_4$ was then added into the cell. The mixture of O_2 (Air Liquide, 99.999%) and one alkane (that is, ethane (Air Liquide, 99.9%), propane (Air Liquide, 99.9%) or methane (Air Liquide, 99.999%)) was directly delivered into the cell through a gas dispersion frit at a total flow rate of 9 standard cubic centimetres per minute. The flow rates of two reactant gases were controlled by mass flow controllers (MKS Instruments) and calibrated by an ADM flow meter (Agilent Technologies). We note that the crystal structure and morphology of post-reaction Cu powder remain unchanged (Supplementary Figs. 1 and 2). The ex situ XPS data show that the post-reaction Cu powder surface is mostly metallic with small amounts of surface oxides (Supplementary Fig. 3).

For control experiments with the absence of ethane or O_2, 80% Ar (Air Liquide, 99.999%) + 20% O_2 or 80% C_2H_6 + 20% Ar was used as the gas feed. For control experiments with H_2O_2 instead of O_2 as the oxidant, 0.2 M H_2O_2 (Alfa Aesar, ACS reagent, 29–32% w/w in H_2O) and a gas feed containing 80% C_2H_6 + 20% Ar were used. For control experiments with Pt and Pd, 20 mg ml^{-1} Pt (Alfa Aesar, amorphous, APS <3 μm, 99.9% metals basis) or Pd powder (Alfa Aesar, spherical, APS 0.5–1.7 μm, 99.95% metals basis) was used as the catalyst. For control experiments with $NaClO_4$ instead of $HClO_4$, the concentration of $NaClO_4$ (Sigma-Aldrich, 99.99% trace metals basis) solution was 1.0 M to keep a consistent ClO_4^- concentration. For control experiments with H_2SO_4 instead of $HClO_4$, the concentration of H_2SO_4 (Sigma-Aldrich, 95.0–98.0% H_2SO_4, 99.999% trace metals basis) solution was 0.5 M to keep a consistent H^+ concentration. For control experiments with weaker acids as the medium, 1.0 M phosphoric acid (Alfa Aesar, ACS reagent, ≥85 wt. % in H_2O) and oxalic acid dihydrate (Alfa Aesar, ≥98.0%) were used. For control experiments using Cu ions instead of Cu powder, an acidic solution composed of 0.18 M Cu^{2+} and 1.0 M ClO_4^- (that is, 0.18 M $Cu(ClO_4)_2$ + 0.64 M $HClO_4$) was used. The concentration of Cu^{2+} was chosen to match the final concentration of Cu^{2+} after ethane activation in 1.0 M $HClO_4$ at 0.2 O_2 mole fraction with 20 mg ml^{-1} Cu powder (Supplementary Table 10). The 0.18 M $Cu(ClO_4)_2$ + 0.64 M $HClO_4$ solution was prepared by dissolving copper(II) perchlorate hexahydrate (Alfa Aesar, 99.999% metals basis) in 0.64 M $HClO_4$. For control experiments with CuO or Cu_2O, 25 mg ml^{-1} CuO (Macklin, 10 μm, 99.9% metals basis) or 22.5 mg ml^{-1} Cu_2O (Adamas, 99%) was used to keep the same loading of Cu element (20 mg ml^{-1}) with 80% C_2H_6 + 20% O_2 or 80% C_2H_6 + 20% Ar as the gas feed.

For ethanol or acetic acid oxidation, ethanol (Aladdin, >99.9%) or acetic acid (Sigma-Aldrich, ≥99.99% trace metals basis) was oxidized using 80% Ar + 20% O_2. The concentration of ethanol and acetic acid in the 1.0 M $HClO_4$ solution was chosen to be 10 mM, similar to total concentration of produced oxygenates in ethane activation under otherwise identical conditions. The carbon balance of the reaction products is close to 100% (Supplementary Fig. 30). The total flow rate of the gas feed in all control experiments was 9 standard cubic centimetres per minute.

For Cu recycling experiments, a homemade glass electrochemical cell was used for the electrochemical deposition of Cu^{2+} ions with a copper foil (Alfa Aesar, 0.1 mm thick, 99.9999% metal basis) as the working electrode and a platinum wire as the counter electrode. The solution from the preceding ethane activation experiments (20 mg ml^{-1} Cu in 1.0 M $HClO_4$ with 80% C_2H_6 + 20% O_2) was used as the electrolyte. The electrochemical deposition was conducted at a constant current density of 200 mA cm^{-2} for 80 min using a Gamry

Reference 600+ potentiostat. The efficiency of Cu recycling was calculated on the basis of the remaining Cu^{2+} concentration. After deposition, the deposited Cu powder was scraped from the Cu foil, rinsed with Milli-Q water and reused as the catalyst for the following ethane activation experiment.

Product quantification

The gas products of alkane activation were quantified every 20 min (30 min for propane activation) by using a gas chromatograph (Agilent 7890B) equipped with a 0.5 m Hayesep Q 80/100 UltiMetal packed column (G3591-81023, Agilent) and a 2 m ShinCarbon ST 80/100 packed column (80486-810901, RESTEK). Ar was used as the carrier gas. The flame ionization detector with a methanizer was used to quantify CO, CH_4, CO_2, C_2H_4, C_2H_6, C_3H_6 and C_3H_8. Flame ionization detector response factors for these species were calibrated by analysing a series of standard gas mixtures.

The liquid products were quantified by using ^{1}H NMR on a Bruker AVIII 600 MHz NMR spectrometer after the reaction. Before NMR sampling, Cu^{2+} ions in the post-reaction solutions were removed via electrolysis to avoid their interference on NMR signals due to their paramagnetism[34]. The NMR sample was then prepared by mixing 500 µl of the processed solution with 100 µl of D_2O (Sigma-Aldrich, 99.9 atom % D) and 50 µM dimethyl sulfoxide (Alfa Aesar, ≥99.9%) as the internal standard. The concentration of dimethyl sulfoxide was calibrated using an acetate anion standard solution (Aladdin, 0.1 mg ml^{-1}). The ^{1}H spectrum was measured with water suppression by using the excitation sculpting method. To identify products formed in alkane activations, NMR spectra of authentic samples of possible products were recorded for comparison (Supplementary Table 11).

The total production rate (r_s) of the activation of one alkane s and the selectivity of product i (S_i) were based on carbon atoms and were calculated as follows:

$$r_s = \frac{1}{v_s}\sum_i r_i v_i \quad (1)$$

$$S_i = \frac{r_i v_i}{r_s v_s} \quad (2)$$

where r_i is the production rate of product i, v_i is the number of carbon atoms in the product i molecule, and v_s is the number of carbon atoms in the substrate (that is, ethane, propane or methane).

To quantify the Cu^{2+} concentration, 200 µl reaction solution was taken out every 10 min from the alkane activation system, diluted to 3 ml using Milli-Q water, and was analysed using ultraviolet–visible spectroscopy (Cary 4000 UV–Vis spectrophotometer). The working curve was generated by analysing a series standard Cu^{2+} sample solutions. In addition, Cu^{2+} concentration measured at the conclusion of the reaction was further verified by weighing the mass loss of Cu powder with a high-precision balance (Mettler Toledo XS105 DualRange) within a difference of less than 3%.

Isotopic labelling study

In $^{13}C_2H_6$ activation experiments, 80% $^{13}C_2H_6$ (Sigma-Aldrich, 99 atom % ^{13}C) + 20% O_2 was used as the gas feed with 20 mg ml^{-1} Cu powder in 1.0 M $HClO_4$. The gas products of ^{13}C-labelled ethane activation were quantified every 20 min using a home-built GC (Agilent 7890B)–MS (Hiden HPR-40) system. The liquid-phase products were analysed in the same way as in $^{12}C_2H_6$ activation. In ethane activation experiments with $^{18}O_2$, 80% C_2H_6 + 20% $^{18}O_2$ (Sigma-Aldrich, 97 atom % ^{18}O) was used as the gas feed with 20 mg ml^{-1} Cu powder in 1.0 M $HClO_4$. As the major gas phase product (that is, ethylene) does not contain oxygen atoms, only liquid products were analysed using the GC–MS QP 2020 ultra system (Shimadzu).

Physical characterizations

SEM images were recorded using a TESCAN VEGA 3 SEM. The accelerating voltage was 10 kV. Powder X-ray diffraction patterns were obtained using a Rigaku MiniFlex 600 with Cu Kα radiation. The Brunauer–Emmett–Teller surface area was measured at −195.8 °C using a Quantachrome Autosorb iQ Station 2. The sample was degassed for 2 h at 300 °C before the measurements. XPS measurements were carried out using a PHI Quantera II with Al Kα radiation. The resulting spectra were analysed using the CasaXPS software package (Casa Software), and peaks were fit using a Gaussian/Lorentzian GL(90) product line shape with the Shirley-type background. The binding energy scale was calibrated by comparing the position of the primary photoelectron peaks in Cu to values in literature[35–37].

In situ SERS

The Raman spectra were recorded using a LabRAM HR Evolution microscope (Horiba Jobin Yvon) equipped with 633 nm laser, a ×50 objective (numerical aperture 0.55), and a charge-coupled device detector. Raman frequencies were calibrated using a Si wafer and ClO_4^- solution spectra. The filter was set to be 50% to keep a low laser intensity to avoid any irradiation-induced modifications of the Cu surface. Each Raman spectrum was acquired over a collection time of 60 s and acquisition number of 2. The Raman spectrum was recorded every 2 min and the recording process lasts for at least 1 h, ensuring the spectra would not change with time. Raman spectra were baseline-corrected if necessary.

A Raman cell with a quartz window was used for all in situ SERS measurements as described in our previous works[38,39]. Cu powder was pressed into a monolithic piece using a hydraulic press at 10 MPa to fit in the Raman cell. The Cu piece was immersed into fresh aqua regia (HCl, ACS reagent, 37%; HNO_3, Alfa Aesar, ~65–70%, 99.999% metals basis) solution for 10 s to remove surface contaminations and then rinsed thoroughly in de-ionized water before experiments.

For collecting Raman spectra of Cu powder under various gaseous atmosphere, 1.0 M $HClO_4$ solution was saturated with pure Ar, O_2, alkanes or their mixtures and delivered into the Raman cell using a peristaltic pump. The solution was cycled and purged continuously with corresponding feeding gas when collecting the spectra.

For collecting Raman spectra of Cu powder with alcohols or iodoalkanes, 50 mM methanol (Sigma-Aldrich, 99.9%), ethanol, 1-propanol (Aladdin, 99.0%), 2-propanol (Sigma-Aldrich, 99.999% trace metals basis), iodomethane (Alfa Aesar, 99.5%, stabilized with copper), iodoethane (Alfa Aesar, 98+%, stabilized with copper), 1-iodopropane (Alfa Aesar, 98+%, stabilized with copper) or 2-iodopropane (Alfa Aesar, 98+%, stabilized with copper) was added into 1.0 M $HClO_4$. For collecting Raman spectra of Cu powder with deuterated iodoalkanes, iodoethane-d_5 (Sigma-Aldrich, 99.5 atom % D, stabilized with copper) and iodomethane-d_3 (Aladdin, 99 atom % D) were used.

Computational details

To simulate the surface of $Cu_2O(111)$ using DFT, we used a slab (3 × 3) consisting of three layers of $Cu_2O(111)$ with the bottom layer fixed in its bulk position. The interaction between atomic cores and valence electrons was calculated using the projector augmented wave method as implemented in Vienna Ab initio Simulation Package (VASP)[40–43]. The exchange–correlation interaction was treated with the Perdew–Burke–Ernzerhof functional[44]. The plane-wave cut-off was set to 400 eV. The semi-empirical D_3 approach as implemented in spin-polarized VASP was employed to describe London dispersion interactions. A Monkhorst–Pack k-point mesh of 4 × 4 × 1 was chosen to sample the reciprocal space[45]. A vacuum of 50 Å was introduced to the supercell to avoid interactions between successive slabs due to the periodic boundary conditions. Each calculation is considered as converged if the electronic energy between two self-consistency steps is smaller than 10^{-4} eV.

To simulate the charged surface interacting with the solvent, we applied the approach proposed by Head-Gordon et al. and Goddard et al.[46–48]. In this approach, the linear Poisson–Boltzmann implicit solvation model with a Debye screening length of 3.0 Å was used to neutralize the non-zero charge in the simulation cell and to simulate water and electrolyte, allowing for a more realistic description of the electrical double layer.

The free energies of the slab systems were calculated as follows:

$$G = E_{\text{elec}}^{\text{solv}} + \text{ZPVE} + H_{\text{vib}} - TS_{\text{vib}} \quad (3)$$

where $E_{\text{elec}}^{\text{solv}}$ is the electronic energy of the system calculated from VASP. All degrees of freedom of the adsorbates were treated as vibrational and neglect the contribution of vibrations of the slab. The vibrational frequencies (ν) were evaluated by calculating the partial Hessian matrix through the finite difference method. Unusually low vibrational modes (<50 cm^{-1}) were corrected to 50 cm^{-1} to avoid unphysically large entropy contributions. Based on the calculated vibrational frequencies, the zero-point vibrational energy (ZPVE), vibrational contributions to the internal energy (H_{vib}) and entropy (S_{vib}) at 298 K (T) were calculated as follows:

$$\text{ZPVE} = \sum_{\nu} \frac{h\nu}{2} \quad (4)$$

$$H_{\text{vib}} = \sum_{\nu} \frac{h\nu}{e^{h\nu/k_B T} - 1} \quad (5)$$

$$S_{\text{vib}} = k_B \sum_{\nu} \left[\frac{h\nu}{k_B T(e^{h\nu/k_B T} - 1)} - \ln(1 - e^{-h\nu/k_B T}) \right] \quad (6)$$

The free energies of the molecules were determined as follows:

$$G = E_{\text{elec}}^{\text{solv}} + \text{ZPVE} + \left(\frac{n}{2} + 1\right) k_B T + H_{\text{vib}} - T(S_{\text{vib}} + S_{\text{trans}} + S_{\text{rot}}) \quad (7)$$

where n is 6 for nonlinear molecules and 5 for linear molecules. ZPVE was calculated as shown above. H_{vib}, S_{vib}, S_{trans} (translational component of entropy), and S_{rot} (rotational component of entropy) were obtained from Jaguar using the Perdew–Burke–Ernzerhof/6-31G* basis set. The free energy of H^+ was estimated from the pK_a of H_3O^+ and the calculated free energies of H_3O^+ and H_2O using the solvation model. A detailed description of this approach has been provided in our previous works[49–51].

The transition state for each reaction was first approached using the nudged elastic band method[52,53]. The plane-wave cut-off, smearing parameter, functional and calculator parameters were the same as those used in slab geometry optimizations. Structures obtained from nudged elastic band were employed to generate the input structure and orientation for the dimer calculation[54]. The force of the dimer calculation was converged to <0.1 eV Å^{-1} to accurately locate the saddle point, that is, the transition state, which were further verified with vibrational frequency analysis. When the calculated free energy barrier is smaller than the corresponding reaction free energy or zero, the reaction free energy is chosen as the free energy barrier.

MD simulations were performed using LAMMPS with ReaxFF force field[55,56]. The reactions of Cu(111) with O_2 were modelled using five layers of 4 × 4 Cu(111) with five O_2 molecules on each side of the vacuum. We used the Nosé–Hoover thermostat and barostat with a damping parameter of 6.25 fs and 125 fs to control the temperature and pressure, respectively. A time step of 0.25 fs was chosen for all MD simulations. We simulated the heating–cooling process using setup as follow: The system was first equilibrated at 300 K for 2.5 ps, followed by increasing the temperature to 500 K in 2.5 ps and then equilibrated at 500 K for 2.5 ps. The system was then heated to 800 K in 2.5 ps and equilibrated for another 2.5 ps. Next, the temperature of O_2 was increased to 1,100 K, while the temperature of Cu was maintained at 800 K to prevent melting. This multi-temperature system was equilibrated for 50 ps. For the cooling process, the temperature of the whole system was decreased to 800 K for 2.5 ps. The temperature was further decreased to 500 K for 2.5 ps and then 300 K for 2.5 ps. After the heating–cooling process, a canonical (NVT) ensemble simulation at 10 K was performed for 2.5 ps.

Data availability

The data supporting the findings of this study are available within the paper and its supplementary information files. All data are available from the corresponding authors upon reasonable request. Source data are provided with this paper.

References

1. Yuan, S. et al. Conversion of methane into liquid fuels—bridging thermal catalysis with electrocatalysis. *Adv. Energy Mater.* **10**, 2002154 (2020).
2. Zhang, H., Li, C., Lu, Q., Cheng, M. J. & Goddard, W. A. III Selective activation of propane using intermediates generated during water oxidation. *J. Am. Chem. Soc.* **143**, 3967–3974 (2021).
3. Galvita, V., Siddiqi, G., Sun, P. & Bell, A. T. Ethane dehydrogenation on Pt/Mg(Al)O and PtSn/Mg(Al)O catalysts. *J. Catal.* **271**, 209–219 (2010).
4. Sun, P., Siddiqi, G., Chi, M. & Bell, A. T. Synthesis and characterization of a new catalyst Pt/Mg(Ga)(Al)O for alkane dehydrogenation. *J. Catal.* **274**, 192–199 (2010).
5. Phadke, N. M., Mansoor, E., Bondil, M., Head-Gordon, M. & Bell, A. T. Mechanism and kinetics of propane dehydrogenation and cracking over Ga/H-MFI prepared via vapor-phase exchange of H-MFI with $GaCl_3$. *J. Am. Chem. Soc.* **141**, 1614–1627 (2019).
6. Sobolev, V. I., Dubkov, K. A., Panna, O. V. & Panov, G. I. Selective oxidation of methane to methanol on a FeZSM-5 surface. *Catal. Today* **24**, 251–252 (1995).
7. Starokon, E. V. et al. Oxidation of methane to methanol on the surface of FeZSM-5 zeolite. *J. Catal.* **300**, 47–54 (2013).
8. Sushkevich, V. L., Palagin, D., Ranocchiari, M. & van Bokhoven, J. A. Selective anaerobic oxidation of methane enables direct synthesis of methanol. *Science* **356**, 523–527 (2017).
9. Periana, R. A. et al. A mercury-catalyzed, high-yield system for the oxidation of methane to methanol. *Science* **259**, 340–343 (1993).
10. Periana, R. A. et al. Platinum catalysts for the high-yield oxidation of methane to a methanol derivative. *Science* **280**, 560–564 (1998).
11. Hashiguchi, B. G. et al. Main-group compounds selectively oxidize mixtures of methane, ethane, and propane to alcohol esters. *Science* **343**, 1232–1237 (2014).
12. Kim, R. S. & Surendranath, Y. Electrochemical reoxidation enables continuous methane-to-methanol catalysis with aqueous Pt salts. *ACS Cent. Sci.* **5**, 1179–1186 (2019).
13. Murahashi, S. I., Oda, Y., Naota, T. & Komiya, N. Aerobic oxidations of alkanes and alkenes in the presence of aldehydes catalyzed by copper salts. *J. Chem. Soc. Chem. Commun.* 139–140 (1993).
14. Komiya, N., Naota, T., Oda, Y. & Murahashi, S.-I. Aerobic oxidation of alkanes and alkenes in the presence of aldehydes catalyzed by copper salts and copper-crown ether. *J. Mol. Catal. A* **117**, 21–37 (1997).
15. Zhao, Y. et al. Speciation of Cu surfaces during the electrochemical CO reduction reaction. *J. Am. Chem. Soc.* **142**, 9735–9743 (2020).
16. Dong, J. C. et al. In situ Raman spectroscopic evidence for oxygen reduction reaction intermediates at platinum single-crystal surfaces. *Nat. Energy* **4**, 60–67 (2018).

17. Chan, H. Y. H., Takoudis, C. G. & Weaver, M. J. Oxide film formation and oxygen adsorption on copper in aqueous media as probed by surface-enhanced Raman spectroscopy. *J. Phys. Chem. B* **103**, 357–365 (1998).
18. Bodappa, N. et al. Early stages of electrochemical oxidation of Cu(111) and polycrystalline Cu surfaces revealed by in situ Raman spectroscopy. *J. Am. Chem. Soc.* **141**, 12192–12196 (2019).
19. Phillips, D. L., Lawrence, B. A. & Valentini, J. J. Substituent effects on gas-phase photodissociation dynamics: resonance Raman spectra of ethyl iodide, isopropyl iodide, and *tert*-butyl iodide. *J. Phys. Chem.* **95**, 9085–9091 (1991).
20. Street, S. C. & Gellman, A. J. FT-IRAS of adsorbed alkoxides: 1-propoxide on Cu(111). *Surf. Sci.* **372**, 223–238 (1997).
21. Jenks, C. J., Bent, B. E., Bernstein, N. & Zaera, F. The chemistry of alkyl iodides on copper surfaces. 1. Adsorption geometry. *J. Phys. Chem. B* **104**, 3008–3016 (2000).
22. Lin, J. L. & Bent, B. E. C-H vibrational mode-softening in alkyl-groups bound to Cu(111). *Chem. Phys. Lett.* **194**, 208–212 (1992).
23. Street, S. C. & Gellman, A. J. Quantitative adsorbate orientation from vibrational spectra: ethoxides on Cu(111). *J. Chem. Phys.* **105**, 7158–7170 (1996).
24. Sung, D. & Gellman, A. J. Ethyl iodide decomposition on Cu(111) and Cu(221). *Surf. Sci.* **551**, 59–68 (2004).
25. Lin, J. L. & Bent, B. E. Carbon halogen bond-dissociation on copper surfaces: effect of alkyl chain length. *J. Phys. Chem.* **96**, 8529–8538 (1992).
26. Lin, J. L. & Bent, B. E. Iodomethane dissociation on Cu(111): bonding and chemistry of adsorbed methyl groups. *J. Vac. Sci. Technol. A* **10**, 2202–2209 (1992).
27. Forbes, J. G. & Gellman, A. J. The β-hydride elimination mechanism in adsorbed alkyl groups. *J. Am. Chem. Soc.* **115**, 6277–6283 (2002).
28. Kao, L. C., Hutson, A. C. & Sen, A. Low-temperature, palladium(II)-catalyzed, solution-phase oxidation of methane to methanol derivative. *J. Am. Chem. Soc.* **113**, 700–701 (1991).
29. Periana, R. A., Mironov, O., Taube, D., Bhalla, G. & Jones, C. J. Catalytic, oxidative condensation of CH_4 to CH_3COOH in one step via CH activation. *Science* **301**, 814–818 (2003).
30. Shan, J., Li, M., Allard, L. F., Lee, S. & Flytzani-Stephanopoulos, M. Mild oxidation of methane to methanol or acetic acid on supported isolated rhodium catalysts. *Nature* **551**, 605–608 (2017).
31. Chua, F. M., Kuk, Y. & Silverman, P. J. Oxygen chemisorption on Cu(110): an atomic view by scanning tunneling microscopy. *Phys. Rev. Lett.* **63**, 386–389 (1989).
32. Dubois, L. H. Oxygen chemisorption and cuprous oxide formation on Cu(111): a high resolution EELS study. *Surf. Sci.* **119**, 399–410 (1982).
33. Chiter, F., Costa, D., Maurice, V. & Marcus, P. DFT-based Cu(111)||Cu_2O(111) model for copper metal covered by ultrathin copper oxide: structure, electronic properties, and reactivity. *J. Phys. Chem. C* **124**, 17048–17057 (2020).
34. Narsimhan, K. et al. Methane to acetic acid over Cu-exchanged zeolites: mechanistic insights from a site-specific carbonylation reaction. *J. Am. Chem. Soc.* **137**, 1825–1832 (2015).
35. Biesinger, M. C. et al. Quantitative chemical state XPS analysis of first row transition metals, oxides and hydroxides. *J. Phys.: Conf. Ser.* 100, 012025 (2008).
36. Biesinger, M. C., Lau, L. W. M., Gerson, A. R. & Smart, R. S. C. Resolving surface chemical states in XPS analysis of first row transition metals, oxides and hydroxides: Sc, Ti, V, Cu and Zn. *Appl. Surf. Sci.* **257**, 887–898 (2010).
37. Zhang, H. et al. Computational and experimental demonstrations of one-pot tandem catalysis for electrochemical carbon dioxide reduction to methane. *Nat. Commun.* **10**, 3340 (2019).
38. He, M. et al. Oxygen induced promotion of electrochemical reduction of CO_2 via co-electrolysis. *Nat. Commun.* **11**, 3844 (2020).
39. Li, C., Xiong, H., He, M., Xu, B. & Lu, Q. Oxyhydroxide species enhances CO_2 electroreduction to CO on Ag via coelectrolysis with O_2. *ACS Catal.* **11**, 12029–12037 (2021).
40. Kresse, G. & Joubert, D. From ultrasoft pseudopotentials to the projector augmented-wave method. *Phys. Rev. B* **59**, 1758–1775 (1999).
41. Hobbs, D., Kresse, G. & Hafner, J. Fully unconstrained noncollinear magnetism within the projector augmented-wave method. *Phys. Rev. B* **62**, 11556–11570 (2000).
42. Kresse, G. & Hafner, J. Ab initio molecular dynamics for liquid metals. *Phys. Rev. B* **47**, 558–561 (1993).
43. Kresse, G. & Hafner, J. Ab initio molecular-dynamics simulation of the liquid-metal-amorphous-semiconductor transition in germanium. *Phys. Rev. B* **49**, 14251–14269 (1994).
44. Perdew, J. P., Burke, K. & Ernzerhof, M. Generalized gradient approximation made simple. *Phys. Rev. Lett.* **77**, 3865–3868 (1996).
45. Monkhorst, H. J. & Pack, J. D. Special points for Brillouin-zone integrations. *Phys. Rev. B* **13**, 5188–5192 (1976).
46. Sundararaman, R. & Goddard, W. A. III The charge-asymmetric nonlocally determined local-electric (CANDLE) solvation model. *J. Chem. Phys.* **142**, 064107 (2015).
47. Goodpaster, J. D., Bell, A. T. & Head-Gordon, M. Identification of possible pathways for C–C bond formation during electrochemical reduction of CO_2: new theoretical insights from an improved electrochemical model. *J. Phys. Chem. Lett.* **7**, 1471–1477 (2016).
48. Sundararaman, R., Goddard, W. A. III & Arias, T. A. Grand canonical electronic density-functional theory: algorithms and applications to electrochemistry. *J. Chem. Phys.* **146**, 114104 (2017).
49. Zhang, H., Goddard, W. A. III, Lu, Q. & Cheng, M. J. The importance of grand-canonical quantum mechanical methods to describe the effect of electrode potential on the stability of intermediates involved in both electrochemical CO_2 reduction and hydrogen evolution. *Phys. Chem. Chem. Phys.* **20**, 2549–2557 (2018).
50. Wu, D., Zhang, J., Cheng, M. J., Lu, Q. & Zhang, H. Machine learning investigation of supplementary adsorbate influence on copper for enhanced electrochemical CO_2 reduction performance. *J. Phys. Chem. C* **125**, 15363–15372 (2021).
51. Chang, K., Zhang, H., Chen, J. G., Lu, Q. & Cheng, M. J. Constant electrode potential quantum mechanical study of CO_2 electrochemical reduction catalyzed by N-doped graphene. *ACS Catal.* **9**, 8197–8207 (2019).
52. Jónsson, H., Mills, G. & Jacobsen, K. W. *in Classical and Quantum Dynamics in Condensed Phase Simulations* (eds Berne, B. J. et al.) 385–404 (World Scientific, 1998).
53. Henkelman, G. & Jónsson, H. Improved tangent estimate in the nudged elastic band method for finding minimum energy paths and saddle points. *J. Chem. Phys.* **113**, 9978–9985 (2000).
54. Henkelman, G. & Jónsson, H. A dimer method for finding saddle points on high dimensional potential surfaces using only first derivatives. *J. Chem. Phys.* **111**, 7010–7022 (1999).
55. van Duin, A. C. T., Dasgupta, S., Lorant, F. & Goddard, W. A. III ReaxFF: a reactive force field for hydrocarbons. *J. Phys. Chem. A* **105**, 9396–9409 (2001).
56. Sengul, M. Y., Randall, C. A. & van Duin, A. C. T. ReaxFF molecular dynamics simulation of intermolecular structure formation in acetic acid-water mixtures at elevated temperatures and pressures. *J. Chem. Phys.* **148**, 164506 (2018).

Acknowledgements

H.Z., C.L., W.L. and Q.L. acknowledge the financial support from the State Key Laboratory of Chemical Engineering (no. SKL-ChE-

23T02) and the Tsinghua University Initiative Scientific Research Program (20211080099). B.X. acknowledges the financial support from Beijing National Laboratory for Molecular Sciences. M.-J.C. acknowledges financial support from the Ministry of Science and Technology of the Republic of China under grant no. MOST 109-2113-M-006-009. W.A.G. acknowledges National Science Foundation (CBET-2005250). All NMR experiments were carried out at the BioNMR Facility, Tsinghua University Branch of China National Center for Protein Sciences (Beijing). We thank N. Xu for the assistance in the NMR data collection. We thank K. Zhao for the insightful discussion on the reaction mechanism. We thank J. Zhang for editing the paper.

Author contributions

H.Z., B.X. and Q.L. designed the project and wrote the paper. H.Z., W.L. and C.L. performed alkane activation experiments and physical characterizations. C.L. and H.Z. conducted the in situ SERS experiments. H.Z. and M.-J.C. performed DFT calculations and MD simulations. W.A.G. and G.L. contributed to data analysis and discussion. Q.L. supervised the entire project.

Competing interests

A patent application (2022100080937) on the alkane activation system based on these results has been filed by Tsinghua University and Peking University with Q.L., H.C., C.L., G.L. and B.X. as inventors.

Additional information

Supplementary information The online version contains supplementary material available at https://doi.org/10.1038/s41929-023-00990-9.

Correspondence and requests for materials should be addressed to Bingjun Xu or Qi Lu.

Peer review information *Nature Catalysis* thanks Wenzhen Li and the other, anonymous, reviewer(s) for their contribution to the peer review of this work.